scientific reports

Check for updates

OPEN

Rotating magnetocaloric effect in highly anisotropic Tb^{III} and Dy^{III} single molecular magnets

Piotr Konieczny[1]✉, Dominik Czernia[1] & Takashi Kajiwara[2]

The magnetocaloric effect (MCE) was investigated in highly anisotropic single crystals of two single molecule magnets (SMMs): $[Ln^{III}(Zn^{II}L)_2]CF_3SO_3$, where Ln = Tb, Dy and L = tripodal hexadentate Schiff base ligand. The structure of these paramagnetic compounds consists of identically oriented linear trinuclear clusters in a trigonal system with an easy direction *c*∥Zn–Ln–Zn array and a hard plane *ab*⊥Zn–Ln–Zn array. The magnitude of MCE measured for *c*∥*H* was significantly greater than MCE for *ab*∥*H* at a wide temperature range regardless of the studied SMM. Therefore, the rotating magnetocaloric effect (RMCE) was evaluated. The maxima of the magnetic entropy change for RMCE were obtained at 2.0 K and moderate fields: 3.9 J K^{-1} kg^{-1} at $\mu_0 H$ = 1.3 T for Ln = Tb and 3.3 J K^{-1} kg^{-1} at $\mu_0 H$ = 1.1 T for Ln = Dy. The relative efficiency of RMCE compared to the MCE measured in *c*∥*H* was as high as 99% at low magnetic fields.

Magnetocaloric effect (MCE) is one of the most promising cooling technology for commercial and cryogenic applications[1]. Magnetic cooling based on MCE is considered a highly efficient and environmentally friendly alternative to the conventional gas compression method[2–4]. Although much research effort is focused on searching high efficient refrigerants near room temperature (for air conditioning or refrigerators)[5–10], the ultra-low temperature range[11–16] is no less important as a cost-effective alternative to ^{3}He dilution refrigerators. The later application will grow in importance as a result of the development of quantum computers which require cryogenic conditions. However, most MCE refrigerants require high magnetic field changes (on the order of $\mu_0 \Delta H \approx 5$–7 T), which is far above the capabilities of modern permanent magnets and therefore limits the application of MCE.

Conventional MCE is a thermodynamic process in which the magnetic material alters its temperature under the change of an external magnetic field[17–21]. However, there is another approach for magnetic cooling that involves the anisotropic magnetocaloric materials, namely the rotating magnetocaloric effect (RMCE)[22–25]. In the conventional MCE, the refrigerant is moving in and out of a magnetic field, or the external magnetic field is applied and removed. In the case of RMCE, aligned single crystals with significant magnetic anisotropy are rotated in a constant magnetic field[17,26–32]. A practical reason for this approach lies in the fact that mechanical rotations of the sample are much easier to perform and more efficient because of the operation at higher frequencies than field sweeps, thus minimizing the number of irreversible heat flows[30,33–35]. Additional energy savings for RMCE can be reached using permanent magnets.

In this work, we present the anisotropic MCE and RMCE studies on two SMM Zn^{II}–Ln^{III}–Zn^{II} trinuclear complexes $[Ln^{III}(Zn^{II}L)_2]CF_3SO_3$, where Ln = Tb (**Tb-SMM**), Dy (**Dy-SMM**) and L denotes a tripodal hexadentate Schiff-base ligand. In our previous works [36,37], it was shown that both compounds are paramagnetic (no long-range magnetic order down to 2.0 K), reveal SMM behavior and have strong magnetic anisotropy with an easy axis along the crystallographic *c* axis which passes through the Zn–Ln–Zn array. The large uniaxial anisotropy makes the studied molecular magnets prospective candidates for RMCE. Single crystal magnetic measurements were performed along the easy axis (*c*∥*H*) and within the hard plane (*ab*∥*H*) to obtain the magnetic entropy change for conventional and rotating magnetocaloric effects. Both compounds reveal large RMCE at 2.0 K in moderate fields, which are easily accessible with permanent magnets.

Results

Both compounds crystallizes in the trigonal crystal system with space group *R*32, with the unit cell parameters of *a* = 11.8682(4) Å, *c* = 38.4392(16) Å, *V* = 4688.9(3) Å^3 for **Tb-SMM** and *a* = 11.9081(4) Å, *c* = 38.2125(18) Å, *V* = 4692.7(3) Å^3 for **Dy-SMM**, respectively[36,37]. The structure consists of two separated ions: a cationic trinuclear cluster $[Ln^{III}(Zn^{II}L)_2]^+$ with rare earth Ln^{III} = Tb^{III}/Dy^{III} as a central ion and a non-magnetic $CF_3SO_3^-$ anion

[1]Institute of Nuclear Physics PAN, Radziwkoskiego 152, 31-342 Kraków, Poland. [2]Department of Chemistry, Faculty of Science, Nara Women's University, Nara 630-8001, Japan. ✉email: piotr.konieczny@ifj.edu.pl

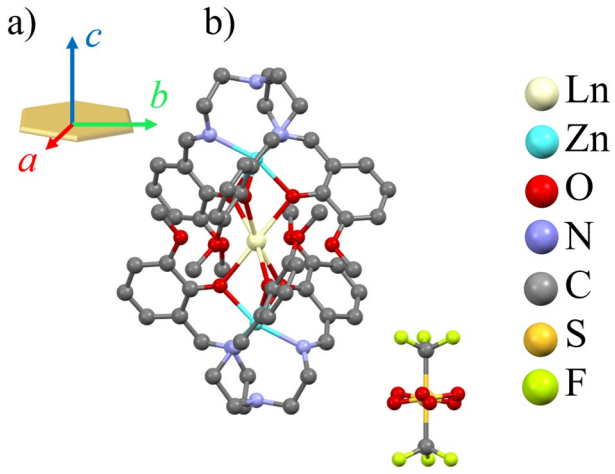

Figure 1. (**a**) The orientation of the monocrystal with the real space directions. (**b**) Crystal structures of the $Ln^{III}(Zn^{II}L)_2$ unit with $Ln^{III} = Tb^{III}$ (**Tb-SMM**), Dy^{III} (**Dy-SMM**) and the $CF_3SO_3^-$ anion. The view is along *a* axis, and hydrogen atoms are omitted for clarity. The $CF_3SO_3^-$ anion is disordered in two positions related by C_2 axis, each with an occupancy of 0.5.

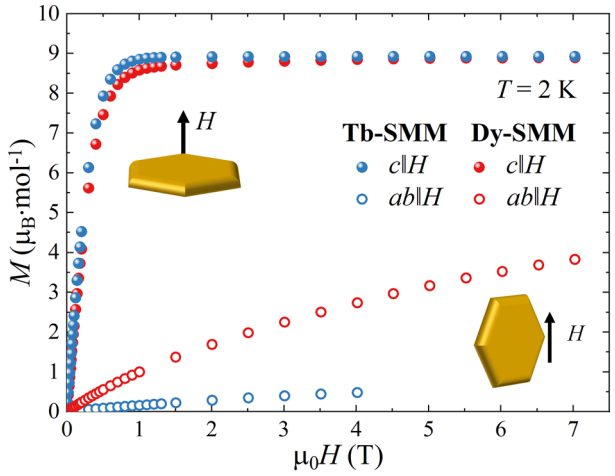

Figure 2. The isothermal magnetization of **Tb-SMM** and **Dy-SMM** at $T = 2.0$ K measured for $ab \| H$ and $c \| H$ orientations in the applied field range $\mu_0 H = 0$–7 T, except for **Tb-SMM** in $ab \| H$, for which the highest field was $\mu_0 H = 4$ T (see "Materials and methods" section). Inset pictures present the orientation of the sample regarding the external field *H*.

(Fig. 1b). A crystallographic three-fold axis passes through the Zn–Tb–Zn array and is parallel to the crystallographic *c* axis. Three two-fold axes are located on $Ln^{III} = Tb^{III}/Dy^{III}$ central ion and are perpendicular to the C_3 axis, and hence the molecule belongs to the D_3 point group symmetry. The coordination sphere around the $Ln^{III} = Tb^{III}/Dy^{III}$ ion is fully occupied by 12 oxygen atoms, with the short-bonded phenoxo oxygen donors (2.3651(19) Å for **Tb-SMM** and 2.3437(19) Å for **Dy-SMM**) at above and below positions and long-attached methoxy oxygen donors (3.0465(15) Å and 3.076(2) Å) located at the equatorial positions. Obtained single crystals were flat and formed the hexagonal-like shape with the crystallographic axis *c* being perpendicular to the surface of the crystal and *ab* crystallographic plane lying in the plane of the surface (Fig. 1a).

Single crystal magnetometry measurements of **Tb-SMM** and **Dy-SMM** were performed within the *ab* plane ($ab \| H$) and along the *c* axis ($c \| H$). Figure 2 shows the isothermal magnetization $M(H)$ of **Tb-SMM** and **Dy-SMM** at $T = 2.0$ K. In both samples, the $c \| H$ is the easy magnetization direction, with saturation magnetization $M_S \approx 8.9$ μ_B mol^{-1}. The crystal field calculation for **Tb-SMM**[36] revealed that in a non-zero magnetic field the lowest lying states of Tb^{3+} ions display maximal values of $\langle J_z \rangle = \pm 6$. Taking into account $g_{Tb} = 3/2$, the expected value of saturation reaches 9 μ_B mol^{-1}, which is close to the measured M_s. In the case of **Dy-SMM** the crystal field analysis[37] revealed that the ground state of the Dy^{3+} ion is degenerated and corresponds to the $|\pm 13/2\rangle$ substates, which points to ≈ 8.7 μ_B mol^{-1} for $g_{Dy} = 4/3$. The *ab* crystallographic plane is the hard magnetization plane with maximum values of 0.5 μ_B mol^{-1} ($\approx 6\%$ of M_S) for **Tb-SMM** at $\mu_0 H = 4$ T and 3.8 μ_B mol^{-1} ($\approx 43\%$ of M_S) for **Dy-SMM** at $\mu_0 H = 7$ T.

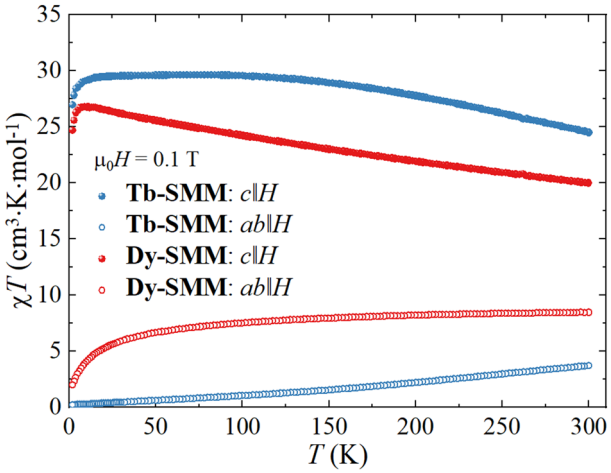

Figure 3. The product of molar magnetic susceptibility and temperature χT for **Tb-SMM** and **Dy-SMM** measured in function of temperature from 300 to 2 K for $c\|H$ and $ab\|H$ orientations in the static magnetic field $\mu_0 H = 0.1$ T.

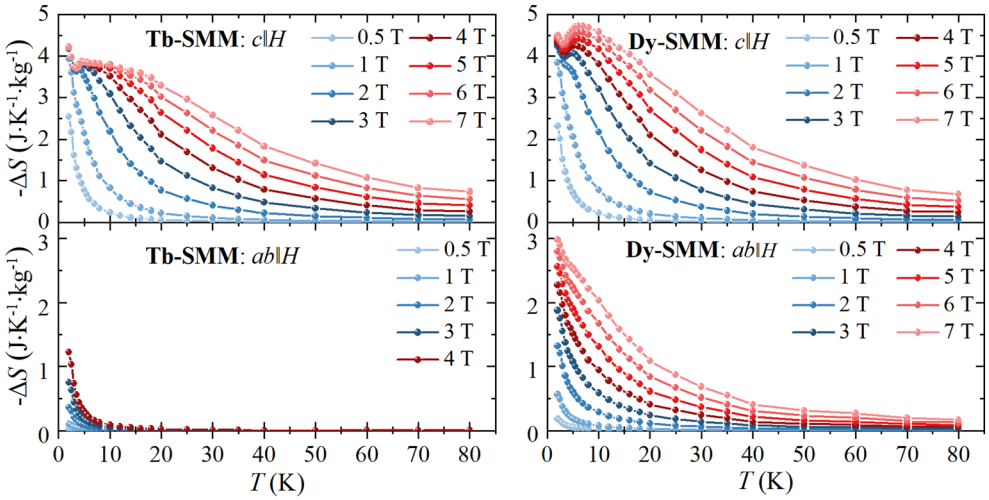

Figure 4. The temperature dependence of entropy change $-\Delta S(T, H)$ for various magnetic field changes for **Tb-SMM** and **Dy-SMM** estimated for the $c\|H$ and $ab\|H$ orientations. Solid lines are guides for the eyes.

The dc magnetic susceptibility $\chi(T)$ was measured during the sample cooling from $T = 300$ K to $T = 2.0$ K in an applied magnetic field of $\mu_0 H = 0.1$ T (Fig. 3). Figure 3 shows the collected data in the form of the χT product for both compounds in $c\|H$ and $ab\|H$. The χT values for **Tb-SMM** and **Dy-SMM** reveal significant differences between the easy axis and the hard plane in the entire temperature range, which point to substantial magnetic anisotropy in both studied compounds (for detailed analysis of magnetic properties, see [36]).

The MCE was evaluated using the indirect method for the isothermal magnetization measurements $M(T, H)$ recorded in the temperature range of $T = 2$–80 K and magnetic field $\mu_0 H$ up to 7.0 T for $ab\|H$ and $c\|H$ orientations (up to 4.0 T for Tb in $ab\|H$ orientation). The magnetic entropy change $\Delta S(T, H)$ was calculated using the Maxwell relationship:

$$\Delta S(T, H) = \mu_0 \int_0^H \left(\frac{\partial M(T, H_1)}{\partial T} \right)_{H_1} dH_1. \quad (1)$$

The $-\Delta S(T, H)$ temperature dependence for selected fields is shown in Fig. 4. A significant difference in MCE was observed between both orientations. The magnitude of MCE was larger for $c\|H$ than for $ab\|H$ for both compounds, and additionally, a peak of the $-\Delta S(T, H)$ appeared for magnetic field $\mu_0 H \geq 3$ T in the case of $c\|H$ but was absent for $ab\|H$. For **Tb-SMM**, the maximum entropy change $-\Delta S_{max}$ was observed at $T = 2.0$ K reaching $-\Delta S_{max} = 4.21$ J K^{-1} kg^{-1} for $c\|H$ in $\mu_0 \Delta H = 7$ T and $-\Delta S_{max} = 1.23$ J K^{-1} kg^{-1} for $ab\|H$ in $\mu_0 \Delta H = 4$ T. In

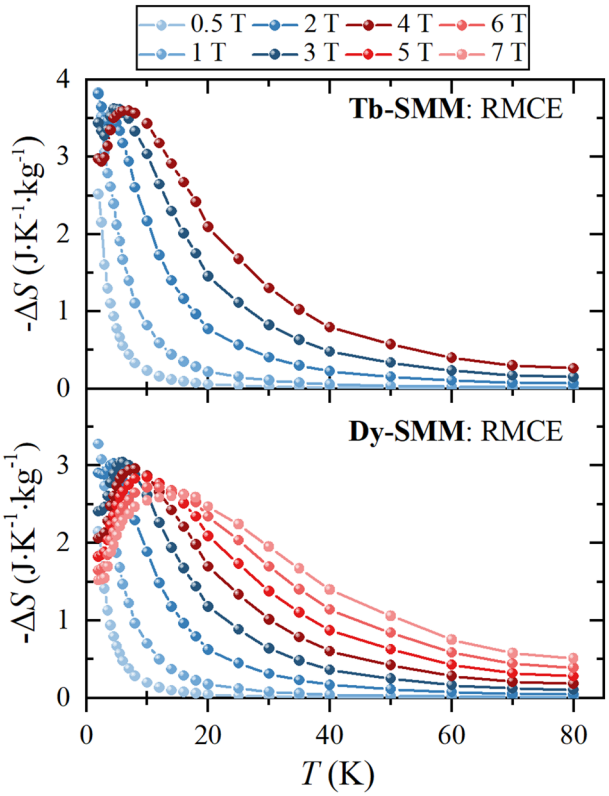

Figure 5. The RMCE entropy change $-\Delta S(T, H)$ as a function of the temperature T ranging from 2 to 80 K for the selected magnetic fields $\mu_0 H$ for **Tb-SMM** and **Dy-SMM**. Solid lines are guides for the eyes.

case of **Dy-SMM** the maximum of $-\Delta S$ was found in $\mu_0\Delta H = 7$ T reaching $-\Delta S_{max} = 4.72$ J K^{-1} kg^{-1} at $T = 6.0$ K for $c\|H$ and $-\Delta S_{max} = 2.98$ J K^{-1} kg^{-1} at $T = 2.0$ K for $ab\|H$.

To study the RMCE, the magnetic entropy change related to the rotation of a single crystal was calculated as the difference $-\Delta S_R = -(\Delta S_c\|_H - \Delta S_{ab}\|_H)$, where $\Delta S_c\|_H$ and $\Delta S_{ab}\|_H$ are the entropy changes for $c\|H$ and $ab\|H$ respectively. Figure 5 depicts $-\Delta S_R$ temperature dependence for **Tb-SMM** and **Dy-SMM**. One can notice the presence of the peak that was also observed for the conventional MCE for $c\|H$, which for the RMCE entropy change is broader. Moreover, the position of this peak has moved towards higher temperatures. The shift was from $T = 4.5$ K to $T = 7.0$ K for $\mu_0 H = 4$ T for **Tb-SMM**, and for **Dy-SMM**, from $T = 5.5$ K to $T = 8.0$ K for $\mu_0 H = 4$ T, and $T = 6.0$ K to $T = 16.0$ K for $\mu_0 H = 7$ T.

Figure 6 shows the RMCE entropy change as a function of the applied magnetic field for selected temperatures for **Tb-SMM** and **Dy-SMM**. The maximum RMCE entropy change $-\Delta S_{max}$ was obtained at $T = 2.0$ K for both compounds for relatively low magnetic fields. For **Tb-SMM**, $-\Delta S_{max}$ was found for $\mu_0 H = 1.3$ T with $-\Delta S_{max} = 3.94$ J K^{-1} kg^{-1}, and for **Dy-SMM** for $\mu_0 H = 1.1$ T with $-\Delta S_{max} = 3.3$ J K^{-1} kg^{-1}. One can notice that the peak of the $-\Delta S$ moves towards higher temperatures with an increasing magnetic field. Therefore, for low magnetic fields, the RMCE is greater at lower temperatures, whereas high fields are more advantageous at higher temperatures. For **Tb-SMM**, in $\mu_0 H = 4$ T, $-\Delta S_{max}$ is found at $T = 7$ K, and for **Dy-SMM** in $\mu_0 H = 7$ T at $T = 14$ K.

The utility of material for magnetocaloric cooling applications can be evaluated using the proposed Temperature averaged Entropy Change (*TEC*) figure of merit [38–41]:

$$TEC(\Delta T_{lift}) = \frac{1}{\Delta T_{lift}} \max_{T_{mid}} \left\{ \int_{T_{mid}-\frac{\Delta T_{lift}}{2}}^{T_{mid}+\frac{\Delta T_{lift}}{2}} |\Delta S(T, H)| dT \right\}. \quad (2)$$

It is estimated for the specific temperature range $\Delta T_{lift} = T_{hot} - T_{cold}$ in which the refrigerating material can potentially work, where T_{hot} and T_{cold} are temperatures of cold and hot reservoirs, respectively. The integral is maximized for the center of the average, T_{mid}, chosen by sweeping over the available $\Delta S(T, H)$ data. In our study, the temperature interval ΔT_{lift} was set between 1 and 30 K with a fixed step of 1 K.

The dependence of *TEC* on ΔT_{lift} in $\mu_0 H = 1$ T, 4 T was depicted in Fig. 7 for **Tb-SMM** and **Dy-SMM** for conventional MCE in $c\|H$ and $ab\|H$ orientations and RMCE. As expected for $ab\|H$, the *TEC* was small compared to the easy axis geometry for both compounds regardless of the magnetic field value. In $\mu_0 H = 1$ T, the *TEC* performances were almost identical in four cases: in $c\|H$ orientation for **Tb-SMM** and **Dy-SMM**, RMCE for **Tb-SMM**, and slightly lower for RMCE for **Dy-SMM** (down to 85% of the corresponding *TEC* for the other three cases). The *TEC* values monotonically decreased with ΔT_{lift} for both compounds and all orientations in the analyzed range. The situation is different in $\mu_0 H = 4$ T, for which the $TEC(\Delta T_{lift})$ curves split. Although for

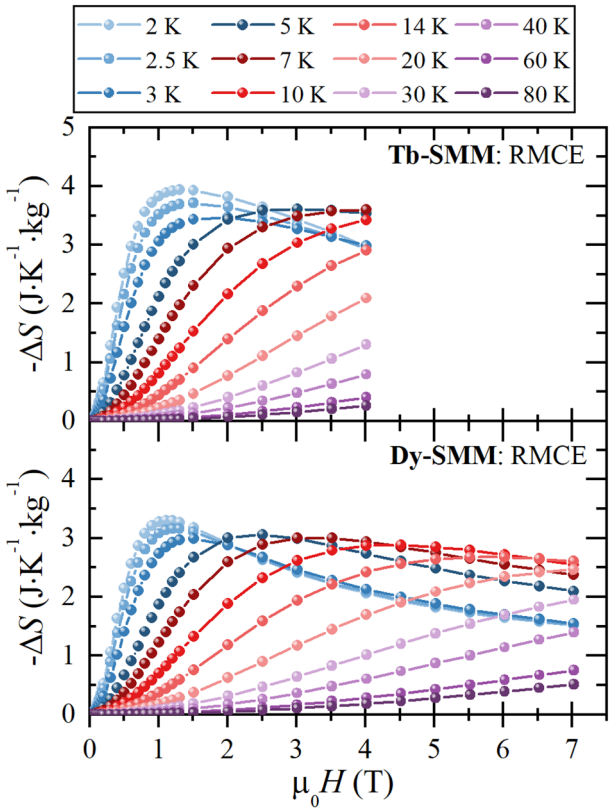

Figure 6. The RMCE entropy change $-\Delta S(T, H)$ as a function of the magnetic field $\mu_0 H$ up to 7 T for the selected temperatures for **Tb-SMM** and **Dy-SMM**. Solid lines are guides for the eyes.

Tb-SMM, the *TEC* for RMCE still amounts to approximately 90% of corresponding *TEC* for $c \| H$ orientation, the same ratio was reduced to 70% for **Dy-SMM**. Additionally, the *TEC* values were relatively constant in the range $\Delta T_{lift} = 1$–6 K for $c \| H$ and RMCE for both SMMs. For larger values of ΔT_{lift}, *TEC* started to decrease linearly.

The temperature interval of $\Delta T_{lift} = 5$ K was selected to study the field dependence of *TEC*(5) for **Tb-SMM** and **Dy-SMM**. The results are presented in Fig. 8. For **Tb-SMM** in $c \| H$ orientation, *TEC* initially increased with the magnetic field up to $\mu_0 H = 4$ T and reached a plateau for higher fields. In $\mu_0 H = 1$ T, *TEC* was equal to 2.46 J K^{-1} kg^{-1}, and in $\mu_0 H = 4$–7 T to 3.83 J K^{-1} kg^{-1}. Similar behavior was observed for RMCE for the same compound, obtaining *TEC* = 2.42 J K^{-1} kg^{-1} in $\mu_0 H = 1$ T and *TEC* = 3.55 J K^{-1} kg^{-1} in $\mu_0 H = 4$ T. In hard geometry, a monotonic increase of *TEC* with the magnetic field was observed with *TEC* = 0.04, 0.48 J K^{-1} kg^{-1} in $\mu_0 H = 1$, 4 T, respectively. For **Dy-SMM** in $c \| H$ orientation, *TEC* increased in the whole magnetic field range reaching *TEC* = 2.38, 4.2, 4.68 J K^{-1} kg^{-1} in $\mu_0 H = 1$, 4, 7 T, respectively. The corresponding *TEC* for RMCE increased with the magnetic field up to $\mu_0 H = 3$ T, and then it started decreasing. The obtained values for RMCE were equal to *TEC* = 2.13, 2.91, 2.61 J K^{-1} kg^{-1} in $\mu_0 H = 1$, 4, 7 T, respectively. As for **Tb-SMM** in hard geometry, the corresponding *TEC* for **Dy-SMM** showed a monotonic increase of *TEC* with magnetic field with *TEC* = 0.26, 1.66, 2.61 J K^{-1} kg^{-1} in $\mu_0 H = 1$, 4, 7 T, respectively.

Discussion

Although the obtained $-\Delta S_{max}$ for **Tb-SMM** and **Dy-SMM** are approximately ten times smaller than the recently reported values for magnetic coolers based on Gd ions with $-\Delta S_{max} = 30$–50 J K^{-1} kg^{-1} in $\mu_0 H = 7$ T [42–44], it should be noted that the RMCE reported in this study brings a few essential advantages. The magnetic fields at which the RMCE exhibits $-\Delta S_{max}$ ($\mu_0 H = 1.3$ T (**Tb-SMM**), 1.1 T (**Dy-SMM**)) are easily accessible by the permanent magnets; therefore, the potential magnetic cooler based on **Tb-SMM** or **Dy-SMM** could operate without superconducting magnets. The RMCE-based refrigerator can also work at higher frequencies and thus with greater efficiency than the conventional MCE. Last but not least, the problem of low heat conductivity and dissipation of the released heat [21] may be overcome due to the flat geometry of the crystals used and thus a large surface-to-volume ratio. The RMCE properties for selected compounds are compared in Table 1. In high field conditions ($\mu_0 H = 5.0$ T) and T_{max} (the temperature at which $-\Delta S$ reaches maximum value), there are many examples of refrigerants revealing giant RMCE, which is much higher than those observed for **Tb-SMM** and **Dy-SMM**. However, from economical point of view, the most interesting conditions are low fields ($\mu_0 H = 1.0$ T, easily accessible with permanent magnets) and $T = 2.0$ K (which can be easily reached by pumping liquid ^{4}He). In these conditions ($\mu_0 H = 1.0$ T and $T = 2.0$ K), both investigated compounds reveal high performance, comparable to other refrigerants with giant RMCE.

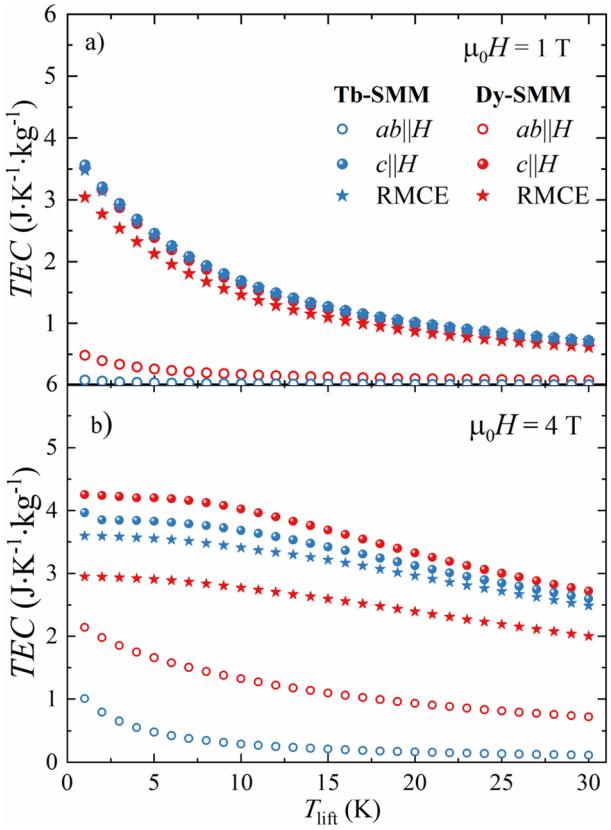

Figure 7. The temperature averaged entropy change (TEC) in the function of temperature interval ΔT_{lift} for conventional MCE and RMCE for **Tb-SMM** and **Dy-SMM** calculated for the applied magnetic field of $\mu_0 H = 1$ T (**a**) and $\mu_0 H = 4$ T (**b**).

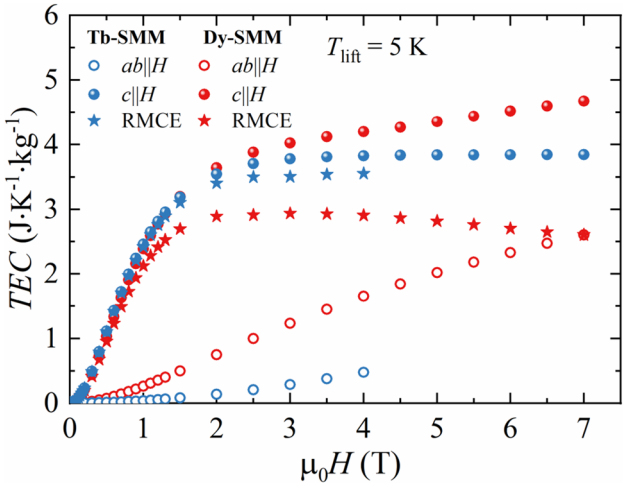

Figure 8. The temperature averaged entropy change (TEC) in the function of applied magnetic field $\mu_0 H$ calculated for temperature interval $\Delta T_{lift} = 5$ K for conventional MCE and RMCE for **Tb-SMM** and **Dy-SMM**.

Recently reported materials for conventional MCE show the variation of $TEC(5)$ in $\mu_0 \Delta H = 1$ T between 1 and 10 J K^{-1} kg^{-1} [41,48–53]; thus, the RMCE results reported for **Tb-SMM** and **Dy-SMM** fall in a moderate range with $TEC(5) = 2.42$ J K^{-1} kg^{-1} for the former and $TEC(5) = 2.13$ J K^{-1} kg^{-1} for the latter in the same magnetic field. The studies of the RMCE in $HoNiGe_3$ single crystal [54] presented a much higher $TEC(5)$ of approximately 12 J K^{-1} kg^{-1} in $\mu_0 \Delta H = 5$ T compared to the corresponding values of 3.55 J K^{-1} kg^{-1} in $\mu_0 H = 4$ T for **Tb-SMM**, and 2.82 J K^{-1} kg^{-1} in $\mu_0 H = 5$ T for **Dy-SMM**, but with significantly smaller entropy change in $\mu_0 \Delta H = 1$ T and

Name	Refs.	$-\Delta S_{max}$ (J K^{-1} kg^{-1})	
		$\mu_0 H = 5.0$ T and T_{max}	$\mu_0 H = 1.0$ T and $T = 2.0$ K
Tb-SMM	This work	3.60 (in $\mu_0 H$ 4.0 T) at 7.0 K	3.83
Dy-SMM	This work	2.85 at 10 K	3.28
Textured DyNiSi	[45]	17.6 at 13 K	≈ 3.5
$TbScO_3$	[46]	23.62 at ≈ 5.0 K	≈ 3.0
$TbMn_2O_5$	[34]	13.14 at ≈ 11 K	≈ 1.8
$\{Dy(OAc)_3(H_2O)_2\}_2]\ 4H_2O$	[30]	≈ 6.0 J K^{-1} kg^{-1} at ≈ 10.0 K	≈ 4.5
$Ni(en)(H_2O)_4SO_4\ 2H_2O$	[47]	≈ 12.0 J K^{-1} kg^{-1} at ≈ 10.0 K	≈ 0.5

Table 1. Examples of rotating magnetocaloric properties of selected potential refrigerants.

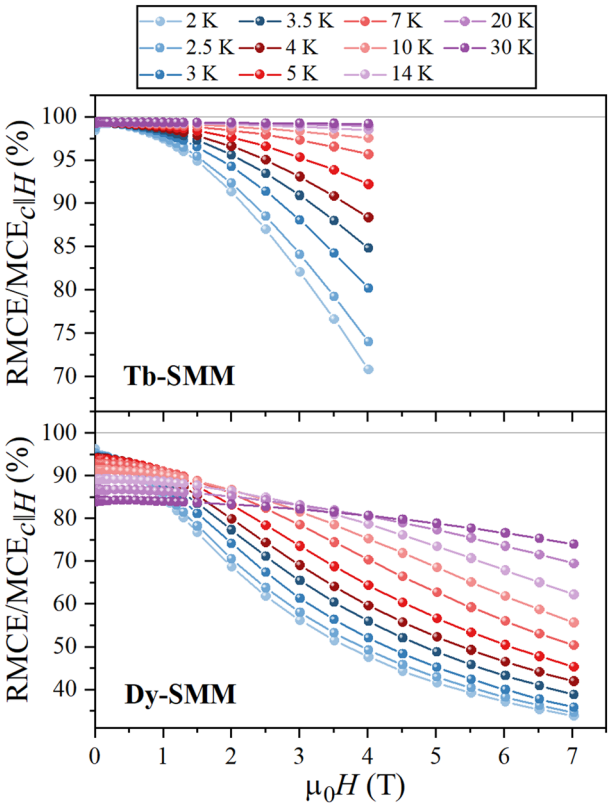

Figure 9. The ratio RMCE/MCE$_c\|_H$ between RMCE and conventional MCE measured for $c\|H$ at $T = 2$–80 K for **Tb-SMM** in magnetic fields up to $\mu_0 H = 4$ T and **Dy-SMM** in fields up to $\mu_0 H = 7$ T. Solid lines are guides for the eyes.

higher temperatures for which the entropy change maximum was observed (between 5 and 15 K). Therefore, **Tb-SMM** and **Dy-SMM** are potentially more attractive candidates for ultra-low temperature cooling with permanent magnets.

The large difference between MCE for $c\|H$ and $ab\|H$ makes the RMCE nearly as efficient as the conventional MCE$_c\|_H$ measured for $c\|H$, what is pictured by the RMCE/MCE$_c\|_H$ ratio in Fig. 9. In the case of **Tb-SMM**, the RCME/MCE$_c\|_H$ value does not drop below the level of 90% for all temperatures measured in the magnetic fields up to $\mu_0 H = 2$ T. Moreover, the ratio increases monotonically with the temperature in the full range of measured fields. The relative efficiency of RMCE is lower for **Dy-SMM**, for which the ratio RCME/MCE$_c\|_H$ was higher than 90% only for $T = 2$–10 K and magnetic fields up to about $\mu_0 H = 1$ T. The difference in RCME/MCE$_c\|_H$ between **Tb-SMM** and **Dy-SMM** is directly related to MCE within the hard plane ($ab\|H$), which is substantially weaker for **Tb-SMM**. Ideally, the RMCE should be the most efficient in a system for which the conventional MCE almost vanishes in one of the crystal orientations and is large for another orientation.

Figure 10 shows field dependence of temperature at which the $-\Delta S_R$ reveals a peak (T_{peak}). The peaks could be observed only under certain conditions: $T = 4.5$–7 K and $\mu_0 H = 2$–4 T for **Tb-SMM** and $T = 4.5$–16 K and $\mu_0 H = 2$–7 T for **Dy-SMM**. For both compounds, the T_{peak} shifts to higher temperatures with increasing the

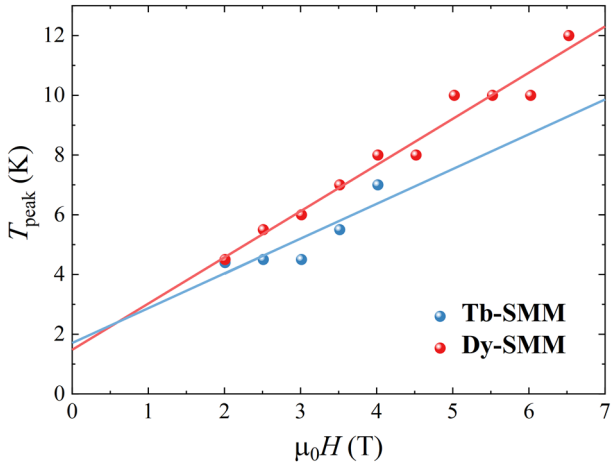

Figure 10. Field dependence of T_{peak} for **Tb-SMM** and **Dy-SMM**. The solid lines are the best fits to the linear function.

magnetic field. Magnetic field splits the energy levels due to the Zeeman splitting. The higher the field, the greater the splitting. In higher fields, stronger thermal fluctuations are required to populate the shifted states. Therefore, the temperature of the T_{peak} is increasing with increasing magnetic field. The solid lines in Fig. 10 represent the best linear fit to the obtained points giving $a = 1.24(40)$ K/T, $b = 1.5(1.2)$ K and $a = 1.55(10)$ K/T, $b = 1.51(46)$ K for **Tb-SMM** and **Dy-SMM** respectively.

Conclusions

The single crystal MCE of Dy^{III} and Tb^{III} based magnetic clusters were investigated in easy direction $c \| H$ and hard plane $ab \| H$. It was shown that the presence of large magnetic anisotropy can have a substantial impact on the magnetic entropy change in two perpendicular orientations. The MCE for $c \| H$ is higher in magnitude than for $ab \| H$ and has a maximum peak, which is not the case for $ab \| H$. Because of these properties, the detailed research of RMCE was done for both studied compounds.

Although **Tb-SMM** reveals lower values of conventional MCE than **Dy-SMM**, regardless of temperature and field conditions, the efficiency of RMCE is greater for **Tb-SMM** due to substantially higher magnetic anisotropy of the Tb compound. The maximum of the entropy change $-\Delta S_{max}$ for RMCE was found at $T = 2.0$ K with $-\Delta S_{max} = 3.94$ J K^{-1} kg^{-1} in $\mu_0 H = 1.3$ T for **Tb-SMM** and $-\Delta S_{max} = 3.3$ J K^{-1} kg^{-1} in $\mu_0 H = 1.1$ T for **Dy-SMM**.

The performance of RMCE evaluated from *TEC* ($T_{lift} = 5$ K) is comparable with conventional MCE in all measured magnetic fields for **Tb-SMM** and up to approximately $\mu_0 H = 1$ T for **Dy-SMM** (the difference between *TEC*s for RMCE and MCE was less than 10%). *TEC*s obtained for **Tb-SMM** and **Dy-SMM** are almost the same up to $\mu_0 H = 1.5$ T, but for higher magnetic fields, **Dy-SMM** outperforms **Tb-SMM** by 9% in $\mu_0 H = 4$ T and 18% in $\mu_0 H = 7$ T based on that figure of merit. However, *TEC* for RMCE indicates that the **Tb-SMM** single crystal is a better material for magnetocaloric cooling, with 12% higher *TEC* in $\mu_0 H = 1$ T and 18% higher *TEC* in $\mu_0 H = 4$ T than the corresponding *TEC* for **Dy-SMM**.

The relative efficiency of RMCE was calculated as the ratio RMCE/$MCE_{c \| H}$ between entropy changes. The best efficiency is obtained at low magnetic fields, reaching almost 100% at all temperatures studied for **Tb-SMM** and 95% at $T = 2.0$ K for **Dy-SMM**. The peak position of the entropy change for RMCE moves towards higher temperatures with increasing magnitude of the magnetic field. The mutual relation between peak position coordinates (temperature, magnetic field) may be described using a linear function.

Materials and methods

The single crystals of **Tb-SMM**[36] and **Dy-SMM**[37] were synthesizedaccording to the literature procedures.

All the magnetic measurements were carried out with the MPMS XL magnetometer from Quantum Design. Single crystals of each compound were aligned in predetermined directions and mounted with Varnish GE adhesive. The plates with the single crystal were attached to a low-signal plastic straw to keep the specified orientation of the sample with respect to the magnetic field.

The studies were performed in two single crystal orientations: $ab \| H$ and $c \| H$. The isothermal magnetization $M(H)$ was collected at $T = 2$–80 K in the field range of $\mu_0 H = 0$–7 T for **Tb-SMM** in the $c \| H$ orientation and **Dy-SMM** for both geometries. The magnetic field range for **Tb-SMM** for $ab \| H$ was reduced to $\mu_0 H = 0$–4 T because the strong magnetic torque leads to breaking the sample in higher fields. The dc magnetic susceptibility $\chi(T)$ was measured during the cooling from $T = 300$ K to $T = 2.0$ K under $\mu_0 H = 0.1$ T. The mass of single crystals was 6.51 mg for **Tb-SMM** and 1.87 mg for **Dy-SMM**. All measurements were corrected for diamagnetic contribution using Pascal's constants[55].

Data availability

The datasets used and/or analyzed during the current study are available from the corresponding author on reasonable request.

Received: 20 July 2022; Accepted: 20 September 2022
Published online: 05 October 2022

References

1. Communication from the Commission to the European Parliament, the Council, the European Economic and Social Committee and the Committee of the Regions on an EU Strategy for Heating and Cooling. (2016).
2. GschneidnerJr, K. A., Pecharsky, V. K. & Tsokol, A. O. Recent developments in magnetocaloric materials. *Rep. Prog. Phys.* **68**, 1479–1539 (2005).
3. Balli, M., Jandl, S., Fournier, P. & Kedous-Lebouc, A. Advanced materials for magnetic cooling: Fundamentals and practical aspects. *Appl. Phys. Rev.* **4**, 021305 (2017).
4. Franco, V. *et al.* Magnetocaloric effect: From materials research to refrigeration devices. *Prog. Mater. Sci.* **93**, 112–232 (2018).
5. Franco, V., Blázquez, J. S., Ingale, B. & Conde, A. The magnetocaloric effect and magnetic refrigeration near room temperature: Materials and models. *Annu. Rev. Mater. Res.* **42**, 305–342 (2012).
6. Zhong, W., Au, C.-T. & Du, Y.-W. Review of magnetocaloric effect in perovskite-type oxides. *Chin. Phys. B* **22**, 057501 (2013).
7. Brück, E. Developments in magnetocaloric refrigeration. *J. Phys. D Appl. Phys.* **38**, R381–R391 (2005).
8. Barua, R. *et al.* Enhanced room-temperature magnetocaloric effect and tunable magnetic response in Ga-and Ge-substituted AlFe2B2. *J. Alloys Compd.* **777**, 1030–1038 (2019).
9. Paramanik, T. & Das, I. Near room temperature giant magnetocaloric effect and giant negative magnetoresistance in Co, Ga substituted Ni–Mn–In Heusler alloy. *J. Alloys Compd.* **654**, 399–403 (2016).
10. El-Gendy, A. A. & Hadjipanayis, G. C. Room temperature magnetocaloric effect in Mn1.25Fe1.75Ga Heusler alloys. *J. Alloys. Compd.* **665**, 319–322 (2016).
11. Flood, D. J. Magnetization and magnetic entropy of Dy 2 Ti 2 O 7. *J. Appl. Phys.* **45**, 4041–4044 (1974).
12. Das, M., Roy, S. & Mandal, P. Giant reversible magnetocaloric effect in a multiferroic GdFeO3 single crystal. *Phys. Rev. B* **96**, 174405 (2017).
13. Pełka, R. *et al.* Magnetocaloric effect in molecular magnet. *J. Magn. Magn. Mater.* **354**, 359–362 (2014).
14. Fitta, M., Pełka, R., Konieczny, P. & Bałanda, M. Multifunctional molecular magnets: Magnetocaloric effect in octacyanometallates. *Crystals (Basel)* **9**, 9 (2018).
15. Evangelisti, M. & Brechin, E. K. Recipes for enhanced molecular cooling. *Dalton Trans.* **39**, 4672 (2010).
16. Torres, F., Hernández, J. M., Bohigas, X. & Tejada, J. Giant and time-dependent magnetocaloric effect in high-spin molecular magnets. *Appl. Phys. Lett.* **77**, 3248–3250 (2000).
17. Konieczny, P., Pełka, R., Czernia, D. & Podgajny, R. Rotating magnetocaloric effect in an anisotropic two-dimensional $Cu^{II}[W^{V}(CN)_8]^{3-}$ molecular magnet with topological phase transition: Experiment and theory. *Inorg. Chem.* **56**, 11971–11980 (2017).
18. *Molecular Magnetic Materials: Concepts and Applications*. (Wiley, 2017).
19. Pecharsky, V. K. & Gschneidner, K. A. Some common misconceptions concerning magnetic refrigerant materials. *J. Appl. Phys.* **90**, 4614–4622 (2001).
20. Li, L.-W. Review of magnetic properties and magnetocaloric effect in the intermetallic compounds of rare earth with low boiling point metals. *Chin. Phys. B* **25**, 037502 (2016).
21. Sessoli, R. Chilling with magnetic molecules. *Angew. Chem. Int. Ed.* **51**, 43–45 (2012).
22. Tarasenko, R., Tkáč, V., Orendáčová, A., Orendáč, M. & Feher, A. Experimental study of the rotational magnetocaloric effect in $KTm(MoO_4)_2$. *Physica B Condens. Matter.* **538**, 116–119 (2018).
23. Moon, J. Y. *et al.* Anisotropic magnetic properties and giant rotating magnetocaloric effect in double-perovskite Tb_2CoMnO_6. *Phys. Rev. B* **98**, 174424 (2018).
24. Skokov, K. P., Pastushenkov, Y. G., Nikitin, S. A., Fries, M. & Gutfleisch, O. Rotational magnetocaloric effect in the $Er_2Fe_{14}B$ single crystal. *IEEE Trans. Magn.* **52**, 1–4 (2016).
25. Beckmann, C., Ehrens, J. & Schnack, J. Rotational magnetocaloric effect of anisotropic giant-spin molecular magnets. *J. Magn. Magn. Mater.* **482**, 113–119 (2019).
26. Nikitin, S. A., Skokov, K. P., Koshkid'ko, Y. S., Pastushenkov, Y. G. & Ivanova, T. I. Giant rotating magnetocaloric effect in the region of spin-reorientation transition in $NdCo_5$ single crystal. *Phys. Rev. Lett.* **105**, 137205 (2010).
27. Jin, J.-L. *et al.* Giant anisotropy of magnetocaloric effect in $TbMnO_3$ single crystals. *Phys. Rev. B* **83**, 184431 (2011).
28. Barua, R. *et al.* Anisotropic magnetocaloric response in $AlFe_2B_2$. *J. Alloys Compd.* **745**, 505–512 (2018).
29. Konieczny, P. *et al.* Self-enhancement of rotating magnetocaloric effect in anisotropic two-dimensional (2D) cyanido-bridged Mn^{II}-Nb^{IV} molecular ferrimagnet. *Inorg. Chem.* **56**, 2777–2783 (2017).
30. Lorusso, G., Roubeau, O. & Evangelisti, M. Rotating magnetocaloric effect in an anisotropic molecular dimer. *Angewandte Chemie Int. Edn.* **55**, 3360–3363 (2016).
31. Konieczny, P. *et al.* Double magnetic relaxation and magnetocaloric effect in the Mn9[W(CN) 8]6(4,4′-dpds)4 cluster-based network. *Inorg. Chem.* **56**, 7089–7098 (2017).
32. Moon, J. Y., Kim, M. K., Choi, Y. J. & Lee, N. Giant anisotropic magnetocaloric effect in double-perovskite Gd_2CoMnO_6 single crystals. *Sci. Rep.* **7**, 16099 (2017).
33. Balli, M., Jandl, S., Fournier, P. & Gospodinov, M. M. Anisotropy-enhanced giant reversible rotating magnetocaloric effect in $HoMn_2O_5$ single crystals. *Appl. Phys. Lett.* **104**, 232402 (2014).
34. Balli, M., Jandl, S., Fournier, P. & Dimitrov, D. Z. Giant rotating magnetocaloric effect at low magnetic fields in multiferroic $TbMn_2O_5$ single crystals. *Appl. Phys. Lett.* **108**, 102401 (2016).
35. Engelbrecht, K. *et al.* Experimental results for a novel rotary active magnetic regenerator. *Int. J. Refrig.* **35**, 1498–1505 (2012).
36. Konieczny, P. *et al.* Anisotropy of spin-lattice relaxations in mononuclear Tb^{3+} single-molecule magnets. *J. Phys. Chem. C* **124**, 7930–7937 (2020).
37. Konieczny, P., Pełka, R. & Kajiwara, T. *submitted* (2022).
38. Griffith, L. D., Mudryk, Y., Slaughter, J. & Pecharsky, V. K. Material-based figure of merit for caloric materials. *J. Appl. Phys.* **123**, 034902 (2018).
39. Choura-Maatar, S. *et al.* Enhancement of the magnetic and magnetocaloric properties by Na substitution for Ca of $La_{0.8}Ca_{0.2}MnO_3$ manganite prepared via the Pechini-type sol–gel process. *J. Mater. Sci. Mater. Electron.* **31**, 1634–1645 (2020).
40. Laajimi, K. *et al.* Large magnetocaloric effect in $0.25(La_{0.67}Ca_{0.33}MnO_3 + La_{0.67}Ca_{0.13}Sr_{0.2}Mn_{0.98}Ni_{0.02}O_3)/0.5\ La_{0.67}Ca_{0.23}Sr_{0.1}Mn_{0.98}Ni_{0.02}O_3$ composite close to room temperature. *Eur. Phys. J. Plus.* **137**, 943 (2022).
41. Zheng, Z. *et al.* Enhancement of magnetic properties and magnetocaloric effects for $Mn_{0.975}Fe_{0.975}P_{0.5}Si_{0.5}$ alloys by optimizing quenching temperature. *Adv. Eng. Mater.* 2200160 (2022).

42. Peng, J.-B. *et al.* A 48-metal cluster exhibiting a large magnetocaloric effect. *Angew. Chem. Int. Ed.* **50**, 10649–10652 (2011).
43. Chang, L.-X., Xiong, G., Wang, L., Cheng, P. & Zhao, B. A 24-Gd nanocapsule with a large magnetocaloric effect. *Chem. Commun.* **49**, 1055–1057 (2013).
44. Song, T. Q. *et al.* Wheel-like Ln_{18} cluster organic frameworks for magnetic refrigeration and conversion of CO_2. *Inorg. Chem.* **57**, 3144–3150 (2018).
45. Zhang, H. *et al.* Giant rotating magnetocaloric effect induced by highly texturing in polycrystalline DyNiSi compound. *Sci. Rep.* **5**, 11929 (2015).
46. Wu, Y.-D. *et al.* Giant conventional and rotating magnetocaloric effects in $TbScO_3$ single crystal. *J. Alloys Compd.* **894**, 162447 (2022).
47. Danylchenko, P. *et al.* Giant rotational magnetocaloric effect in $Ni(en)(H_2O)_4{\cdot}2H_2O$: Experiment and theory. *Magnetochemistry* **8**, 39 (2022).
48. Guo, D., Moreno-Ramírez, L. M., Law, J.-Y., Zhang, Y. & Franco, V. Excellent cryogenic magnetocaloric properties in heavy rare-earth based $HRENiGa_2$ (HRE = Dy, Ho, or Er) compounds. *Sci. China Mater.* https://doi.org/10.1007/s40843-022-2095-6 (2022).
49. Wang, Y., Guo, D., Wu, B., Geng, S. & Zhang, Y. Magnetocaloric effect and refrigeration performance in $RE_{60}Co_{20}Ni_{20}$ (RE = Ho and Er) amorphous ribbons. *J. Magn. Magn. Mater.* **498**, 166179 (2020).
50. Xie, H. *et al.* Giant and reversible low field magnetocaloric effect in $LiHoF_4$ compound. *Dalton Trans.* **50**, 17697–17702 (2021).
51. Dong, Z., Wang, Z. & Yin, S. Magnetic properties and magneto-caloric effect (MCE) in $Cu_{22}Al_{18}Ho_{22}Tm_{20}Gd_{18}$ amorphous ribbons. *J. Magn. Magn. Mater.* **514**, 167270 (2020).
52. Zhang, Y. *et al.* Magnetic properties, magnetocaloric effect and refrigeration performance in $RE_{60}Al_{20}Ni_{20}$ (RE = Tm, Er and Ho) amorphous ribbons. *J. Appl. Phys.* **127**, 033905 (2020).
53. Xie, H. *et al.* Enhanced low-field magnetocaloric effect in Nb and Al co-substituted $EuTiO_3$ compounds. *J. Mater. Sci. Technol.* **118**, 128–135 (2022).
54. Zhao, X. *et al.* Anisotropic magnetocaloric effect and magnetoresistance in antiferromagnetic $HoNiGe_3$ single crystal. *Intermetallics (Barking)* **138**, 107307 (2021).
55. Bain, G. A. & Berry, J. F. Diamagnetic corrections and Pascal's constants. *J. Chem. Educ.* **85**, 532–536 (2008).

Acknowledgements

The present research was financed by National Science Centre (Poland) Grant SONATA No. (2018/31/D/ST8/02118).

Author contributions

P.K.: study design, perform experiment, data analysis and interpretation, manuscript preparation; D.C.: data collection and analysis, manuscript preparation; T.K.: sample synthesis, structure details, manuscript preparation.

Competing interests

The authors declare no competing interests.

Additional information

Correspondence and requests for materials should be addressed to P.K.

Reprints and permissions information is available at www.nature.com/reprints.

Publisher's note Springer Nature remains neutral with regard to jurisdictional claims in published maps and institutional affiliations.